PHYSICAL REVIEW B VOLUME 56, NUMBER 23 15 DECEMBER 1997-I

# Quantum transport in square and triangular antidot arrays with various periods

Satoshi Ishizaka
*NEC Fundamental Research Laboratories, 34 Miyukigaoka, Tsukuba, Ibaraki 305, Japan*

Tsuneya Ando
*Institute for Solid State Physics, University of Tokyo, 7-22-11 Roppongi, Minato-ku, Tokyo 106, Japan*

(Received 19 June 1997)

Quantum effects on electron transport in square and triangular antidot arrays are studied in a self-consistent Born approximation based on full-quantum-mechanical energy bands. When the array period is large and the Fermi wavelength is comparable to the antidot diameter, a quantum effect increases the effective antidot diameter and shifts some commensurability peaks toward magnetic fields different from classical ones. When the array period is small, the Hall conductivity is reduced due to the appearance of magnetic minibands giving a quantized value opposite to that of the usual Landau levels and the commensurability peak is significantly enhanced. The Aharonov-Bohm–type oscillation superimposed on the commensurability peak changes its feature with the decrease of the period. [S0163-1829(97)06847-1]

## I. INTRODUCTION

Lateral surface superlattices with a strong electrostatic potential modulation are called antidot arrays, where two-dimensional electron gas (2DEG) at the GaAs/Al$_x$Ga$_{1-x}$As heterostructure cannot penetrate into the high potential antidot region. In such antidot arrays, oscillations in magnetoresistances have been observed such as the commensurability oscillation and the Aharonov-Bohm (AB) –type oscillation. The purpose of the present paper is to clarify quantum effects on these oscillations in square and triangular arrays.

The resistivity in antidot arrays exhibits a peak around a magnetic field satisfying the commensurability conditions $2r_c/a=1,\ \sqrt{2},\ \dots,$ where $r_c$ is the classical cyclotron radius and $a$ is the period of the antidot array. This commensurability oscillation has been widely observed in square antidot arrays,[1–15] whose period and antidot diameter ($d$) run over the wide range ($a=200\ \text{nm}\sim 2\ \mu\text{m}$, $d=100\ \text{nm}\sim 700$ nm). It has also been observed in various geometrical modulations (triangular,[16–23] rectangular,[18,21–26] recursively structured,[16,27] and disordered arrays[19,23,28–30]).

An AB-type oscillation has been observed superimposed on the commensurability peak in antidot arrays having a small array period or large aspect ratio $d/a$.[8,9,26] A large Altshuler-Aronov-Spivak (AAS) oscillation has also been observed in triangular antidot arrays in weak magnetic fields,[20,31] although it will not be discussed in the following. Many theoretical works have been reported for the purpose of understanding these interesting phenomena.[3,32–54]

In a GaAs/Al$_x$Ga$_{1-x}$As heterostructure with a typical electron concentration the Fermi wavelength is 50–60 nm. This indicates that there are only several one-dimensional channels between neighboring antidots in arrays with a small aspect ratio and quantum effects play important roles in various phenomena as well as causing the AB-type and AAS oscillations. In fact, the commensurability peak itself is significantly modified by quantum effects.[39,50] Furthermore, when the Fermi wavelength becomes comparable to the antidot diameter at an extremely low electron concentration, quantum effects can appear even in an array having a small aspect ratio or a large period.

In this paper, we numerically calculate the conductivity tensor of square and triangular antidot arrays in a self-consistent Born approximation[57] (SCBA) using full-quantum-mechanical energy bands and varying the aspect ratio in a systematic manner. The results are compared with those obtained in classical calculations. In Sec. II, we briefly show the method used for the numerical calculations. In Sec. III, we show and discuss the numerical results in square antidot arrays. In Sec. IV, we investigate the case of the triangular antidot arrays. A summary and conclusion are given in Sec. V.

## II. MODEL FOR ANTIDOT ARRAYS

For square antidot arrays, the Hamiltonian to which the electrons in 2DEG are assumed to be subjected are the same as that in Ref. 55. For triangular antidot arrays, the electrostatic potential describing the antidots is defined in a Wigner-Seitz cell by[51,52]

$$V(x,y)=U_0\left|\cos\left(\frac{\pi(\sqrt{3}x+y)}{2a}\right)\cos\left(\frac{\pi y}{a}\right)\times\cos\left(\frac{\pi(\sqrt{3}x-y)}{2a}\right)\right|^{4\beta/3}. \tag{2.1}$$

We assume the situation that the antidot diameter is fixed at 100 nm and the steepness parameter $\beta$ is changed depending on the array period, whose values are listed in Table I in Ref. 55.

The conductivity tensor is calculated by the Kubo formula[56] in a SCBA method,[57] where we assume a quantum-number-independent self-energy for short-range scatterers.[58–60,39,36] The scattering strength is characterized by a mean free path given by $l_e=v_F\tau$, where $v_F$ is the Fermi velocity. Those conductivity tensors are compared with that obtained from the classical Kubo formula,[56] whose results

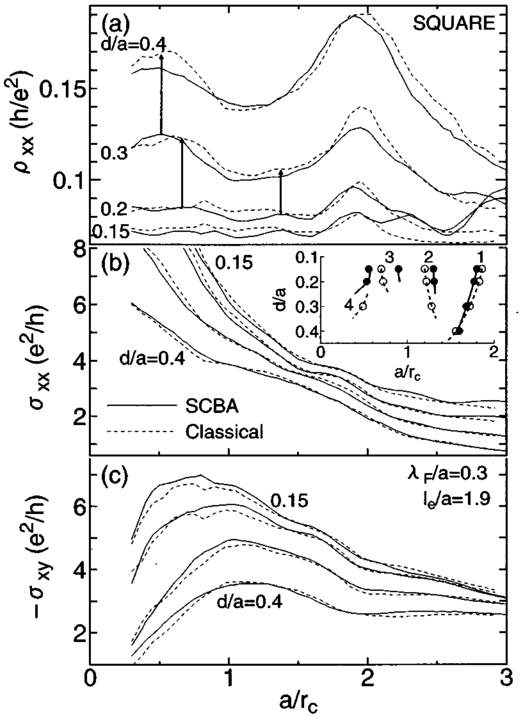

FIG. 1. Calculated (a) $\rho_{xx}$, (b) $\sigma_{xx}$, and (c) $-\sigma_{xy}$ for square arrays with $d/a \leqslant 0.4$. The quantum results obtained in SCBA and classical Monte Carlo results are shown by the solid and dotted lines, respectively. The peak positions in $\sigma_{xx}$ are plotted in the inset of (b). Each curve of $\sigma_{xx}$ is shifted successively by $0.5 \times e^2/h$.

for square antidot arrays with various periods have been already shown in Ref. 55. In order to rigidly compare the results in this paper, the phenomenological relaxation time used in the classical calculation $\tau'$ is determined so as to coincide with that expected from the imaginary part of the averaged self-energy in the SCBA calculation. Namely, we choose $\tau'$ in such a way that

$$\frac{\hbar}{\tau'} = \frac{\hbar}{\tau} \frac{\mathcal{A}(E_F)}{L^2} \sim \langle \mathrm{Im}\Sigma(E_F) \rangle, \tag{2.2}$$

where $L$ is a linear dimension and $\mathcal{A}(E_F)$ is the area in which electrons are allowed to exist classically at the Fermi energy.

It has been pointed out that the fluctuation in the antidot potential can be quite large in actual antidot arrays.[51,49] The conductivity tensor is calculated without explicitly taking into account such antidot fluctuations except that the effective relaxation time is chosen to be considerably shorter than that for an unpatterned GaAs/Al$_x$Ga$_{1-x}$As heterostructure. We shall use $l_e/a = 1.9$ for almost all calculations.

## III. SQUARE ARRAYS

### A. Commensurability peaks

Figure 1 shows calculated results for relatively small aspect ratios. The solid lines are obtained in SCBA at $T=4$ K and the dotted lines by the classical simulation at $T=0$. In the calculation the Fermi wavelength is scaled by the array period as $\lambda_F/a = 0.3$. This gives $\lambda_F = 60$ nm for $d/a = 0.5$ corresponding to situations of existing experiments, but $\lambda_F = 150$ nm for $d/a = 0.2$, which corresponds to electron concentrations smaller than those of usual experiments but is suitable for clarification of quantum effects.

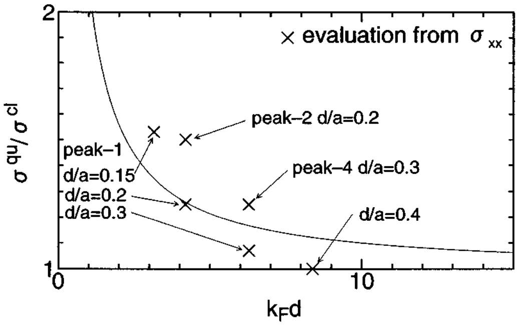

FIG. 2. The transport cross section normalized by the classical value $(4/3)d$ as a function of $k_F d$ for a hard-wall antidot. The values estimated by the position shift in $\sigma_{xx}$ peaks are also plotted.

Quantum-mechanical and classical results are qualitatively quite similar. Many peak structures appear in the diagonal conductivity $\sigma_{xx}$ and resistivity $\rho_{xx}$. The magnetic-field positions of some peaks are shifted with the increase of $d/a$.[55] If we make a detailed comparison between the quantum-mechanical and classical results for $\rho_{xx}$, we notice some differences: When $d/a = 0.2$, quantum $\rho_{xx}$ has three commensurability peaks at $a/r_c \sim 0.7$, 1.3, and 1.9 (the peaks at $a/r_c \sim 2.3$ and 3 are essentially a Shubnikov–de Haas oscillation). The peaks at $a/r_c \sim 0.7$ and 1.3 do not agree with those of the classical $\rho_{xx}$ for the same aspect ratio, but they are closer to corresponding classical peaks for $d/a = 0.3$. Similarly, the quantum peak at $a/r_c = 0.5$ for $d/a = 0.3$ is close to the classical peak for $d/a = 0.4$. These correspondences are shown by arrows in Fig. 1(a). Further, only two commensurability peaks are resolved in quantum $\rho_{xx}$ for $d/a = 0.3$ as in classical $\rho_{xx}$ for $d/a = 0.4$, while three peaks are resolved in classical $\rho_{xx}$ even for $d/a = 0.3$.

The inset of Fig. 1 shows the peak positions of $\sigma_{xx}$ as a function of $d/a$. The peaks of quantum $\sigma_{xx}$'s tend to be shifted toward classical ones with larger $d/a$. It is noteworthy that both classical and quantum-mechanical results give the first commensurability peak for $\rho_{xx}$ at the same magnetic field independent of $d/a$. This is highly likely to be just a coincidence because a structure appearing in $\rho_{xx}$ is determined by those of $\sigma_{xx}$ and $\sigma_{xy}$ in a complicated way depending on their relative importance.[55]

When the aspect ratio is small, it is natural to regard the antidots as scatterers with a small diameter $(\sim d)$.[53] Classically we have $\sigma = (4/3)d$, where $\sigma$ is the transport cross section defined as

$$\sigma = \int_{-\pi}^{\pi} \sigma(\theta)(1-\cos\theta)d\theta, \tag{3.1}$$

with $\sigma(\theta)$ being the differential cross section. Quantum mechanically, the cross section is enhanced over the classical one because of diffraction effects. Figure 2 shows the quantum cross section as a function of $k_F d$ for a hard-wall antidot, where $k_F$ is the Fermi wave number. It contains also effective antidot diameters for quantum results determined

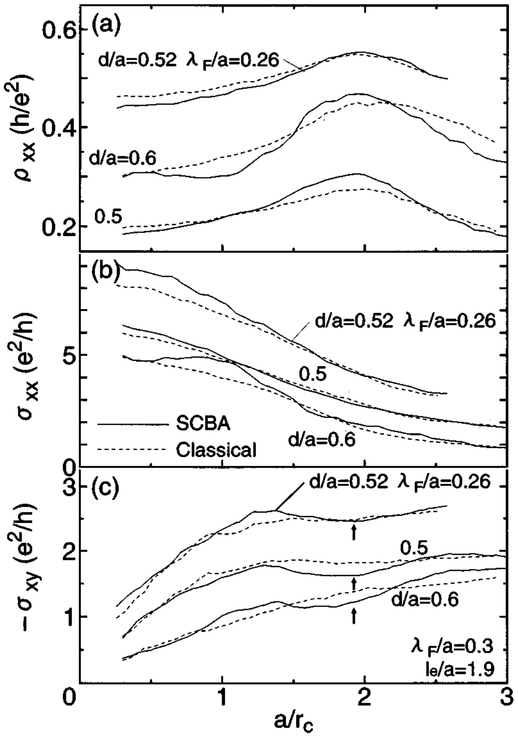

FIG. 3. Calculated (a) $\rho_{xx}$, (b) $\sigma_{xx}$, and (c) $-\sigma_{xy}$ in square arrays with $d/a=0.5$ and 0.6. $\rho_{xx}$ and $\sigma_{xx}$ for $d/a=0.6$ are shifted by $0.1\times h/e^2$ and $e^2/h$, respectively. $\rho_{xx}$, $\sigma_{xx}$, and $-\sigma_{xy}$ for $\lambda_F/a=0.26$ are shifted by $0.3\times h/e^2$, $2\times e^2/h$, and $0.5\times e^2/h$, respectively.

from the data given in the inset of Fig. 1 and the correspondences given by the arrows in Fig. 1(a). It is clear that essential features of the quantum results can be understood in terms of the enhancement in the effective antidot diameter.

Three commensurability peaks are resolved and their positions are close to corresponding classical results for $d/a=0.3$ in a previous calculation made within a similar approximation scheme.[36] There is an important difference in the Fermi wavelength between the previous and present calculation, i.e., $\lambda_F/a=0.3$ in the latter case while $\lambda_F/a=0.16$ in the former case. The quantum effect is emphasized considerably in arrays with large Fermi wavelength.

Figure 3 shows results for systems with a larger aspect ratio ($0.5\leqslant d/a\leqslant 0.6$). It contains also results for a shorter Fermi wavelength $\lambda_F/a=0.26$ and $d/a=0.52$. Classical $\sigma_{xx}$ and $\sigma_{xy}$ have essentially no structures and, therefore, only a very broad peak appears in classical $\rho_{xx}$. The important feature common to all the results is the appearance of a dip in quantum $\sigma_{xy}$ around $a/r_c\sim 2$. As a result quantum $\rho_{xx}$ exhibits a large commensurability peak at $a/r_c\sim 2$. For $d/a=0.6$ some broad feature appears in quantum $\sigma_{xx}$, which further enhances the commensurability peak of $\rho_{xx}$.

When a periodic potential is introduced in magnetic fields, each Landau level splits into different magnetic minibands depending on $\Phi/\Phi_0$, with $\Phi$ being the flux per unit cell defined by $\Phi=Ba^2$ and $\Phi_0$ the flux quantum defined by $\Phi_0=ch/e$.[61] When the potential modulation is weak, the energy spectrum has a fractal character known as Hofstadter's butterfly.[61] The quantized value of the Hall conductivity of each magnetic miniband for the fractal spectrum can take various integers negative or positive.[62] A relation between the broken fractal spectrum and the classical chaotic dynamics has been pointed out.[63]

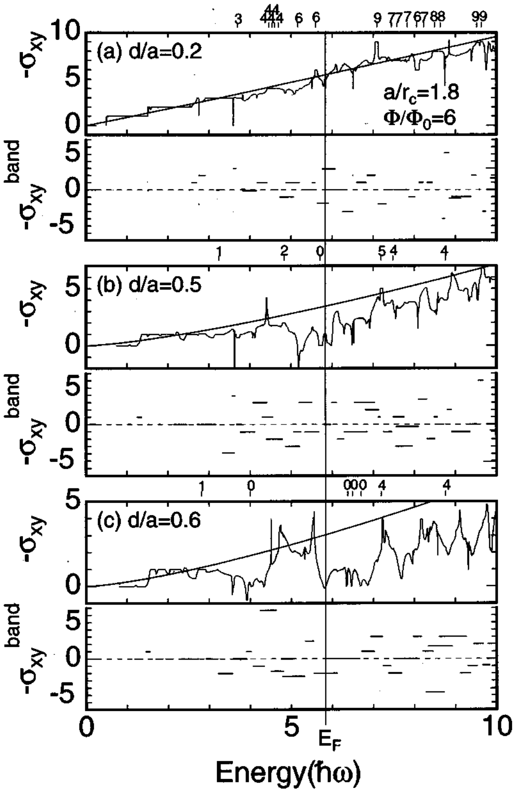

FIG. 4. Calculated Hall conductivity without any disorder at zero temperature in square arrays at a magnetic field corresponding to $\Phi/\Phi_0=6$. The quantized value of the Hall conductivity of each magnetic miniband is shown at the bottom of each panel. The vertical line indicates the Fermi energy.

In Fig. 4, we show calculated Hall conductivity in the absence of scattering for $\Phi/\Phi_0=6$ ($a/r_c=1.8$ for the Fermi energy $E_F/\hbar\omega=5.8$), in which each Landau level splits into six magnetic minibands. The quantized Hall conductivity of each magnetic miniband ($\sigma_{xy}^{\rm band}$) is shown in the lower panel of each figure (each horizontal line corresponds to the width of each magnetic miniband). Many magnetic minibands overlap each other,[34] but some small energy gaps are still present. The positions and quantized values of the total Hall conductivity in these small energy gaps are shown above each figure.

With the increase of the energy, the quantized Hall conductivity of minibands starts to fluctuate and takes both positive and negative values. For small aspect ratio $d/a=0.2$ the fluctuation is not so big and consequently the total Hall conductivity stays almost the same as the ''ideal'' value $-\sigma_{xy}=nec/B$, where $n$ is the electron concentration obtained by using $\mathcal{A}(E)$. With the increase of $d/a$, the fluctuation becomes larger and many minibands giving a negative value for quantized $-\sigma_{xy}^{\rm band}$ appear. As a result the Hall conductivity becomes much smaller than the ideal value.

Figure 5 gives the distribution of minibands giving a positive (open circle) and negative (closed circle) $-\sigma_{xy}^{\rm band}$ together with corresponding energy spectra. This distribution is obtained by averaging over minibands whose energy sepa-

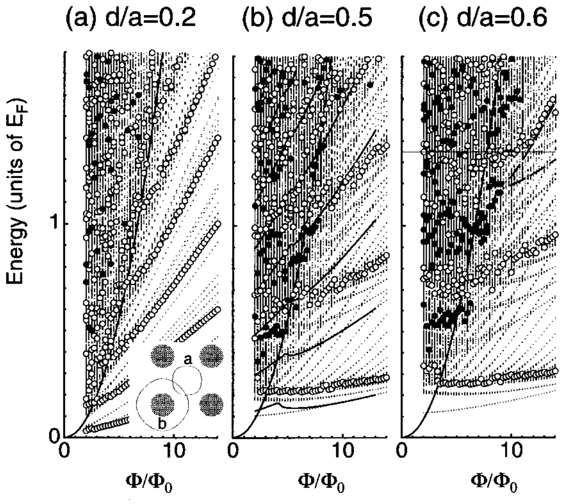

FIG. 5. Magnetic minibands in square arrays. The closed and open circles indicate the minibands with negative and positive quantized Hall conductivity, respectively. The parabolic line in each panel indicates the condition $a/r_c=2$. The energy levels associated with periodic orbit $a$ shown in the inset are shown in (b). The horizontal line in (c) gives the Fermi energy corresponding to $d/a=0.52$ and $\lambda_F/a=0.26$ shown in Fig. 3. The dashed lines in (c) give examples of minibands associated with different Landau levels.

ration is less than $0.075\times E_F$. The figure contains a parabola corresponding to the condition $a/r_c=2$ and semiclassically quantized energy levels (only for $d/a=0.5$) associated with periodic orbit $a$ localized in a space surrounded by four neighboring antidots[18] as illustrated in the inset.

First, we notice that in high magnetic fields the minibands contributing to a positive $-\sigma_{xy}^{\rm band}$ are distributed regularly. With the decrease of the field for a fixed energy, the distribution starts to be less regular. This magnetic field roughly corresponds to that given by the condition that minibands belonging to different Landau levels start to cross each other and, therefore, their mixing becomes appreciable. An example of such two magnetic minibands are shown by dashed lines in Fig. 5(c). This magnetic field is slightly higher than that given by the condition $a/r_c=2$ for $d/a=0.6$, similar for $d/a=0.5$, and smaller for $d/a=0.2$. Bands contributing to a negative quantized value of $-\sigma_{xy}^{\rm band}$ begin to appear at similar magnetic fields. The reduction of $-\sigma_{xy}$ due to the presence of such minibands is not recovered by minibands lying higher in energy and giving a positive contribution to $-\sigma_{xy}^{\rm band}$ even for larger $E_F$. In fact, the results for $d/a=0.52$ and $\lambda_F/a=0.26$ shown in Fig. 3 corresponds to the Fermi energy given by the horizontal line in Fig. 5.

The actual Hall conductivity rapidly deviates from this band Hall conductivity with the decrease of the magnetic field due to the presence of scattering. This is presumably the reason that the reduction in the Hall conductivity disappears in Fig. 3 below $a/r_c\sim1.5$ in spite of the presence of minibands giving negative $-\sigma_{xy}^{\rm band}$ even in such weak magnetic fields.

### B. Aharonov-Bohm–type oscillation

In Fig. 6, calculated $\rho_{xx}$ at $T=1$ K is shown by solid lines for square arrays. An AB-type oscillation appears for all aspect ratios. The density of states (DOS) has also an oscillatory structure and its peak positions are indicated by solid triangles. The positions of the Landau levels without a potential modulation are shown by open triangles. The conductivities $\sigma_{xx}$ and $\sigma_{xy}$ also have a fine oscillation, although they are not explicitly shown here. The results for $d/a=0.5$ are the same as those discussed previously.[39]

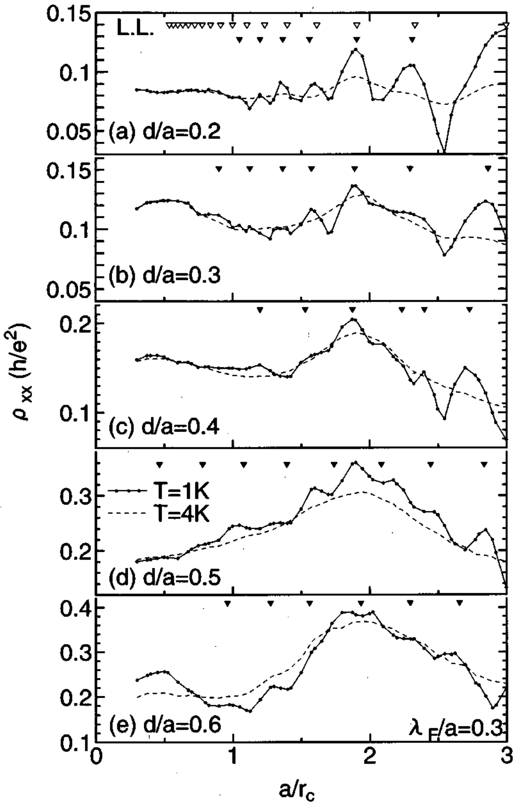

FIG. 6. Calculated $\rho_{xx}$ at $T=1$ K in square arrays. The peak position of DOS is indicated by solid triangles and the position of Landau levels in the absence of a potential modulation is shown by open triangles in (a).

When $d/a=0.2$, the peak position of $\rho_{xx}$ around $a/r_c\sim2$ coincides with that of the density of states (DOS) peak and is very close to that of a Landau level. In this case we have $|\sigma_{xy}|\gg\sigma_{xx}$ and $|\sigma_{xy}|$ has a dip at the DOS peak. These are the feature expected in the usual Shubnikov–de Haas (SdH) oscillation in systems without a potential modulation.[57] For lager aspect ratios, $d/a=0.3$ and 0.4, the oscillatory behavior remains to be that of an SdH oscillation, although the amount of the positional shift from the Landau level becomes significant and the form of the oscillation becomes less regular.

For arrays with $d/a=0.5$, the phase of the oscillation of $\rho_{xx}$ is completely opposite to that of DOS around $a/r_c\sim2$. In fact, $|\sigma_{xy}|$ tends to have a peak at the DOS peak around $a/r_c\sim2$ quite in contrast to the conventional SdH behavior.[39] The correlation between DOS and $\rho_{xx}$ seems to be recovered for $d/a=0.6$, except for a few peaks of $\rho_{xx}$ in the vicinity of $a/r_c=2$. Note, however, that $\sigma_{xx}>|\sigma_{xy}|$ even in this case contrary to the expected SdH behavior $\sigma_{xx}<|\sigma_{xy}|$ as in the case of $d/a=0.2$.

Figure 7 shows the relaxation time dependence of the oscillation. When $d/a=0.2$, the oscillation amplitude for $l_e/a=1.9$ and $l_e/a=3.3$ are almost the same. In the case of

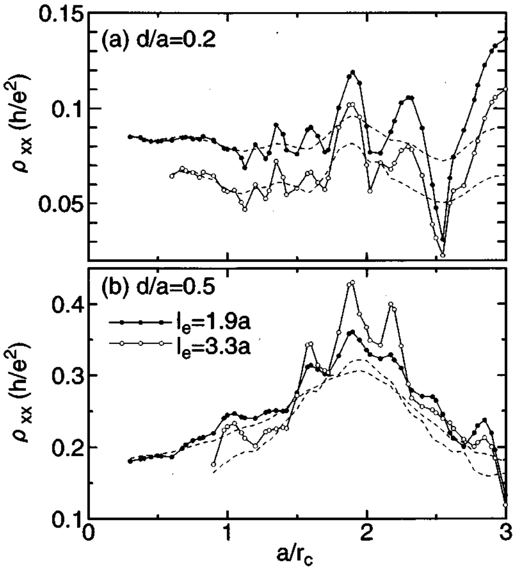

FIG. 7. $\rho_{xx}$ in square arrays with (a) $d/a=0.2$ and (b) $d/a=0.5$ for two values of the electron mean free path.

$d/a=0.5$, however, the oscillation amplitude is quite sensitive to the relaxation time and becomes about a half when the mean free path is reduced from $l_e/a=3.3$ to 1.9, in a qualitative agreement with a previous calculation.[49] These results suggest that the AB-type oscillation changes its qualitative feature from that of an SdH oscillation for $d/a<0.4$ to that of a new oscillation for $d/a>0.4$.

There are various possible mechanisms giving such quantum oscillations. Energy levels obtained by a semiclassical quantization of periodic orbits lead to peaks in both DOS and $\sigma_{xx}$ and dips in $-\sigma_{xy}$.[41,42,39] The level repulsion between runaway orbits contributing greatly to the diffusion and quantized periodic orbits may give rise to an oscillation of the conductivity out of phase with DOS.[39] A quasiperiodic change in the band structure with period $\Phi_0$ related to the Hofstadter butterfly spectrum may also contribute to observable oscillations.[37] It is likely that the actual AB oscillation is a result of a complicated combination of such different mechanisms.

## IV. TRIANGULAR ARRAYS

Figure 8 shows calculated results for triangular arrays (solid lines, SCBA at $T=4$ K; dotted lines, classical at $T=0$). For a small aspect ratio ($d/a=0.2$), many commensurability peaks appear in $\sigma_{xx}$ together with a step-function-like structure in $\sigma_{xy}$ qualitatively in agreement with the case of square arrays. The big difference lies in the fact that the first peak is rapidly shifted to the lower-magnetic-field side with the increase of $d/a$, which is much more appreciable in quantum results. In fact the first peak in quantum $\sigma_{xx}$ seems to merge into the second peak already for $d/a=0.3$, while classical $\sigma_{xx}$ has separate two peaks. The difference between quantum and classical results can again be understood essentially in terms of a quantum enhancement of the effective antidot diameter.

It is interesting to note that the position of the first commensurability peak in $\rho_{xx}$ is shifted to the lower-field side in contrast to the case of square arrays in which the first peak stays at $a/r_c\sim 2$ independent of $d/a$. This big difference in the behavior of the first commensurability peak arises presumably because orbits contributing to the diffusion coefficient most are easily disturbed by the presence of other antidots in triangular arrays. In fact, a simple consideration for a hard-wall antidot shows that the orbit starts to be influenced already for $d/a>(\sqrt{3}-1)/2\approx 0.37$ in the triangular case in contrast to $d/a>2/3\approx 0.67$ in the square case as is shown in the inset of Fig. 8(a).

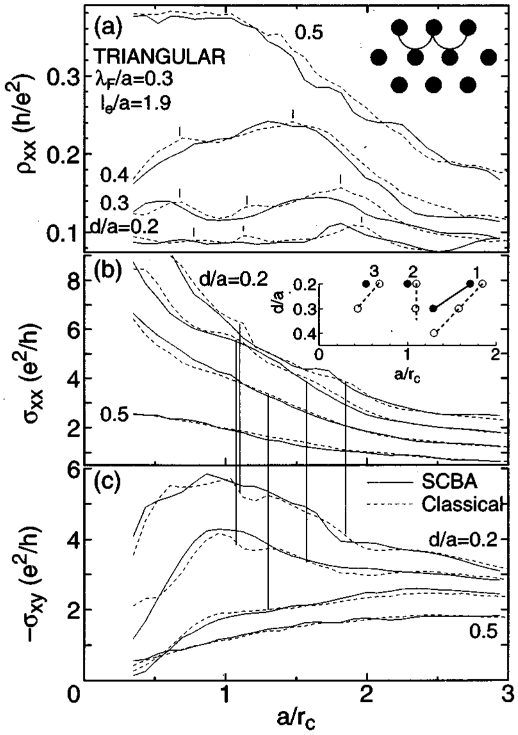

FIG. 8. Calculated (a) $\rho_{xx}$, (b) $\sigma_{xx}$, and (c) $-\sigma_{xy}$ in triangular arrays. Each curve of $\sigma_{xx}$ is shifted successively by $0.5\times e^2/h$.

When $d/a=0.5$, both quantum-mechanical and classical $\rho_{xx}$ have no commensurability peaks. Furthermore, there is no significant difference between quantum and classical $\sigma_{xx}$ and $\sigma_{xy}$. Calculations of the band Hall conductivity reveal that minibands giving a negative $-\sigma_{xy}^{\mathrm{band}}$ appear also in triangular arrays, but they always lie close to minibands with a positive $-\sigma_{xy}$. They tend to cancel each other and, therefore, a reduction in the quantum Hall conductivity at $a/r_c\sim 2$ is absent in triangular arrays.

It should be noted that three commensurability peaks appearing in classical $\rho_{xx}$ at $a/r_c=1.95$, 1.12, and 0.78 agree well with the experimental results given in Refs. 16, 17, and 18, where these three peaks are denoted by 1, 3, and 7, respectively. In these experiments, the Fermi wavelength is much shorter than that used in the present calculation and quantum effects are much weaker.

In Fig. 9, $\rho_{xx}$ at $T=1$ K is shown by solid lines for triangular arrays. For $d/a=0.2$ and 0.3 the peak in the oscillation of $\rho_{xx}$ coincides with that of DOS and this oscillation is qualitatively explained as an SdH oscillation. For $d/a=0.4$ the oscillation of $\rho_{xx}$ starts to have a phase different from that of DOS and for $d/a=0.5$ it has a completely opposite

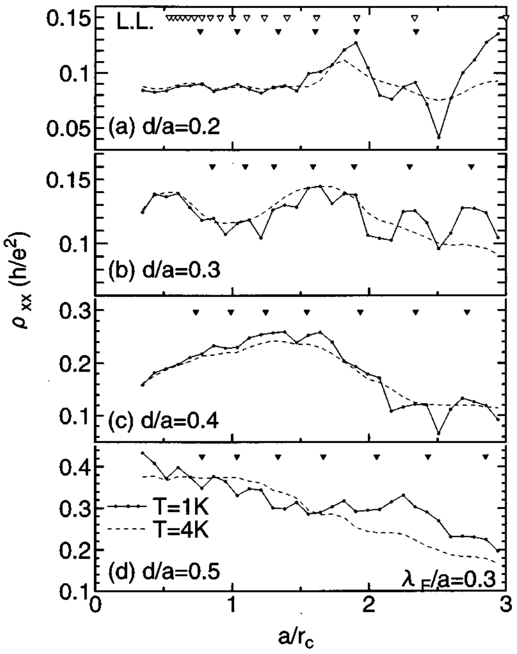

FIG. 9. Calculated $\rho_{xx}$ in triangular arrays at $T=1$ K.

phase. Therefore, the oscillation changes its qualitative behavior at $d/a \sim 0.4$. Although results are not shown explicitly here, the antiphase oscillation observed for large $d/a$ sometimes disappears and turns into an SdH-like oscillation when the Fermi energy is changed. Further, calculations show that the periodic orbit $b$ surrounding an antidot is more stable in triangular arrays than in square arrays and consequently the corresponding DOS oscillation is larger.

## V. SUMMARY

We have calculated the conductivity tensor and magnetoresistivity in square and triangular antidot arrays by systematically varying the aspect ratio in a self-consistent Born approximation and compared them with those of a classical calculation. The results are summarized as follows.

In arrays with a small aspect ratio, an antidot can be regarded as an almost independent scatterer with a small cross section. When the Fermi wavelength becomes large and comparable to the antidot diameter, the effective diameter of an antidot is enhanced over the classical value due to diffraction effects. As a result, the position of the quantum commensurability peaks is shifted toward the peak position in the classical system with a larger aspect ratio. This quantum effect is common to square and triangular arrays.

In strong magnetic fields, the Hall conductivity becomes dominated by $\sigma_{xy}^{\text{band}}$ determined by magnetic minibands. With the decrease of the magnetic field, minibands begin to overlap each other and the mixing causes the appearance of bands giving a negative quantized value of $-\sigma_{xy}$. In square arrays this occurs roughly at $a/r_c \sim 2$ for a large aspect ratio, leading to a reduction in the Hall conductivity and an enhancement of the commensurability peak of the resistivity. For arrays with a smaller aspect ratio, such minibands appear only in weaker magnetic fields where the Hall conductivity is no longer determined by the quantized values of minibands because of strong scattering effects and such quantum effects are not important. In triangular arrays, they are always accompanied by minibands giving a positive value and quantum effects are again not important.

At low temperatures, fine oscillations appear being superimposed on the commensurability peak. The oscillation has a character similar to a Shubnikov–de Haas oscillation for arrays with a small aspect ratio, i.e., it has a phase the same as that of the density of states. For arrays with a large aspect ratio, the oscillation tends to have a phase opposite to that of the density of states. The crossover occurs around $d/a = 0.4$. The oscillation of the former type seems to be more important in triangular arrays.

## ACKNOWLEDGMENTS

We would like to thank F. Nihey, T. Nakanishi, S. Uryu, and O. Sugino for helpful discussions. This work is supported in part by a Grant-in-Aid for Scientific Research on Priority Area, ''Mesoscopic Electronics: Physics and Technology'' from the Ministry of Education, Science and Culture.

---

[1] D. Weiss, M. L. Roukes, A. Menschig, P. Grambow, K. von Klitzing, and G. Weimann, Phys. Rev. Lett. **66**, 2790 (1991).

[2] D. Weiss, P. Grambow, K. von Klitzing, A. Menschig, and G. Weimann, Appl. Phys. Lett. **58**, 2960 (1991).

[3] A. Lorke, J. P. Kotthaus, and K. Ploog, Phys. Rev. B **44**, 3447 (1991).

[4] G. M. Gusev, Z. D. Kvon, V. M. Kudryashov, L. V. Litvin, and Y. V. Nastaushev, Pis'ma Zh. Éksp. Teor. Fiz. **54**, 369 (1991) [ JETP Lett. **54**, 364 (1991)].

[5] G. M. Gusev, Z. D. Kvon, L. V. Litvin, Y. V. Nastaushev, A. K. Kalagin, and A. I. Toropov, Pis'ma Zh. Éksp. Teor. Fiz. **55**, 129 (1992) [ JETP Lett. **55**, 123 (1992)].

[6] G. M. Gusev, Z. D. Kvon, L. V. Litvin, Y. V. Nastaushev, A. K. Kalagin, and A. I. Toropov, J. Phys. Condens. Matter **4**, L269 (1992).

[7] G. M. Sundaram, N. J. Bassom, R. J. Nicholas, G. J. Rees, P. J. Heard, P. D. Prewett, J. E. F. Frost, G. A. C. Jones, D. C. Peacock, and D. A. Ritchie, Phys. Rev. B **47**, 7348 (1993).

[8] F. Nihey and K. Nakamura, Physica B **184**, 398 (1993).

[9] D. Weiss, K. Richter, A. Menschig, R. Bergmann, H. Schweizer, and K. von Klitzing, Phys. Rev. Lett. **70**, 4118 (1993).

[10] K. Nakamura, S. Ishizaka, and F. Nihey, Physica B **197**, 144 (1994).

[11] T. Deruelle, B. Meurer, Y. Guldner, J. P. Vieren, R. Rick, D. Weiss, K. von Klitzing, K. Eberl, and K. Ploog, Phys. Rev. B **49**, 16 561 (1994).

[12] R. Schuster, K. Ensslin, D. Wharam, S. Kühn, J. P. Kotthaus, G. Böhm, W. Klein, G. Tränkle, and G. Weimann, Phys. Rev. B **49**, 8510 (1994).

[13] R. Schuster, G. Ernst, K. Ensslin, M. Entin, M. Holland, G. Böhm, and W. Klein, Phys. Rev. B **50**, 8090 (1994).

[14] K. Tsukagoshi, T. Nagao, M. Haraguchi, S. Takaoka, K. Murase,

and K. Gamo, J. Phys. Soc. Jpn. **65**, 1914 (1996).

[15] K. Tsukagoshi, T. Nagao, M. Haraguchi, S. Takaoka, K. Murase, and K. Gamo, Superlattices Microstruct. (to be published).

[16] J. Takahara, T. Kakuta, T. Yamashiro, Y. Takagaki, T. Shiokawa, K. Gamo, S. Namba, S. Takaoka, and K. Murase, Jpn. J. Appl. Phys. **30**, 3250 (1991).

[17] T. Yamashiro, J. Takahara, Y. Takagaki, K. Gamo, S. Namba, S. Takaoka, and K. Murase, Solid State Commun. **79**, 885 (1991).

[18] D. Weiss, K. Richter, E. Vasiliadou, and G. Lütjering, Surf. Sci. **305**, 408 (1994).

[19] K. Tsukagoshi, S. Wakayama, K. Oto, S. Takaoka, K. Murase, and K. Gamo, Superlattices Microstruct. **16**, 295 (1994).

[20] F. Nihey, S. W. Hwang, and K. Nakamura, Phys. Rev. B **51**, 4649 (1995).

[21] J. Takahara, A. Nomura, K. Gamo, S. Takaoka, K. Murase, and H. Ahmed, Jpn. J. Appl. Phys. **34**, 4325 (1995).

[22] K. Tsukagoshi, M. Haraguchi, K. Oto, S. Takaoka, K. Murase, and K. Gamo, Jpn. J. Appl. Phys. **34**, 4335 (1995).

[23] K. Tsukagoshi, M. Haraguchi, S. Takaoka, and K. Murase, J. Phys. Soc. Jpn. **65**, 811 (1996).

[24] K. Ensslin, S. Sasa, T. Deruelle, and P. M. Petroff, Surf. Sci. **263**, 319 (1992).

[25] R. Schuster, K. Ensslin, J. P. Kotthaus, M. Holland, and C. Stanely, Phys. Rev. B **47**, 6843 (1993).

[26] R. Schuster, K. Ensslin, J. P. Kotthaus, G. Böhm, and W. Klein, Phys. Rev. B **55**, 2237 (1997).

[27] G. M. Gusev, P. Basmaji, D. I. Lubyshev, L. V. Litvin, Y. V. Nastaushev, and V. V. Preobrazhenskii, Phys. Rev. B **47**, 9928 (1993).

[28] G. M. Gusev, Z. D. Kvon, L. V. Litvin, Y. V. Nastaushev, A. K. Kalagin, and A. I. Toropov, Superlattices Microstruct. **13**, 263 (1993).

[29] G. M. Gusev, P. Basmaji, Z. D. Kvon, L. V. Litvin, Y. V. Nastaushev, and A. I. Toropov, J. Phys. Condens. Matter **6**, 73 (1994).

[30] K. Tsukagoshi, S. Wakayama, K. Oto, S. Takaoka, K. Murase, and K. Gamo, Phys. Rev. B **52**, 8344 (1995).

[31] F. Nihey, M. A. Kastner, and K. Nakamura, Phys. Rev. B **55**, 4085 (1997).

[32] R. Fleischmann, T. Geisel, and R. Ketzmerick, Phys. Rev. Lett. **68**, 1367 (1992).

[33] E. M. Baskin, G. M. Gusev, Z. D. Kvon, A. G. Pogosov, and M. V. Entin, Pis'ma Zh. Éksp. Teor. Fiz. **55**, 649 (1992) [ JETP Lett. **55**, 678 (1992)].

[34] H. Silberbauer, J. Phys. Condens. Matter **4**, 7355 (1992).

[35] R. B. S. Oakeshott and A. MacKinnon, J. Phys. Condens. Matter **5**, 6991 (1993).

[36] H. Silberbauer and U. Rössler, Phys. Rev. B **50**, 11 911 (1994).

[37] R. B. S. Oakeshott and A. MacKinnon, J. Phys. Condens. Matter **6**, 1519 (1994).

[38] T. Yamauchi, Phys. Lett. A **191**, 317 (1994).

[39] S. Ishizaka, F. Nihey, K. Nakamura, J. Sone, and T. Ando, Phys. Rev. B **51,** 9881 (1995).

[40] S. Ishizaka, F. Nihey, K. Nakamura, J. Sone, and T. Ando, Jpn. J. Appl. Phys. **34**, 4317 (1995).

[41] K. Richter, Europhys. Lett. **29**, 7 (1995).

[42] G. Hackenbroich and F. von Oppen, Europhys. Lett. **29**, 151 (1995).

[43] I. V. Zozoulenko, F. A. Maao, and E. H. Hauge, Phys. Rev. B **51**, 7058 (1995).

[44] T. Nagao, J. Phys. Soc. Jpn. **64**, 4097 (1995).

[45] T. Nagao, J. Phys. Soc. Jpn. **65**, 2606 (1996).

[46] I. V. Zozoulenko, F. A. Maao, and E. H. Hauge, Phys. Rev. B **53**, 7987 (1996).

[47] I. V. Zozoulenko, F. A. Maao, and E. H. Hauge, Phys. Rev. B **53**, 7975 (1996).

[48] L. Wenchang (unpublished).

[49] S. Uryu and T. Ando, Phys. Rev. B **53**, 13 613 (1996).

[50] S. Uryu and T. Ando, in *23rd International Conference on Physics of Semiconductors*, edited by M. Scheffler and R. Zimmermann (World Scientific, Singapore, 1996), p. 1505.

[51] T. Nakanishi and T. Ando, Phys. Rev. B **54**, 6021 (1996).

[52] T. Nakanishi and T. Ando, Physica B **227**, 127 (1996).

[53] T. Ando, S. Uryu, S. Ishizaka, and T. Nakanishi, Chaos, Solitons Fractals **8**, 1057 (1997).

[54] I. V. Zozoulenko, Frank A. Maaø, and E. H. Hauge, Phys. Rev. B **56**, 4710 (1997).

[55] S. Ishizaka and T. Ando, Phys. Rev. B **55**, 16 331 (1997).

[56] R. Kubo, J. Phys. Soc. Jpn. **12**, 1 (1957).

[57] T. Ando, A. B. Fowler, and F. Stern, Rev. Mod. Phys. **54**, 437 (1982).

[58] C. Zhang and R. R. Gerhardts, Phys. Rev. B **41**, 12 850 (1990).

[59] R. R. Gerhardts, D. Weiss, and U. Wulf, Phys. Rev. B **43**, 5192 (1991).

[60] D. Pfannkuche and R. R. Gerhardts, Phys. Rev. B **46**, 12 606 (1992).

[61] D. Hofstadter, Phys. Rev. B **14**, 2239 (1976).

[62] D. J. Thouless, M. Kohmoto, M. P. Nightingale, and M. den Nijis, Phys. Rev. Lett. **49**, 405 (1982).

[63] T. Geisel, J. Wagenhuber, P. Niebauer, and G. Obermair, Phys. Rev. Lett. **64**, 1581 (1990).